



Integrating CO₂ reduction, H₂O oxidation and H₂ evolution catalysts into a dual S-scheme artificial photosynthetic system for tunable syngas production

Zhixin Fan^a, Yilin Cai^a, Zhenyu Yang^a, Xi Zhang^a, Ruowen Shao^a, Shuxian Zhong^b,
Leihong Zhao^a, Dong Liu^{c,d}, Song Bai^{a,*}

^a Key Laboratory of the Ministry of Education for Advanced Catalysis Materials, College of Chemistry and Materials Science, Zhejiang Normal University, Jinhua, Zhejiang 321004, China

^b College of Geography and Environmental Sciences, Zhejiang Normal University, Jinhua, Zhejiang 321004, China

^c Key Laboratory of Precision and Intelligent Chemistry, School of Chemistry and Materials Science, University of Science and Technology of China, Hefei, Anhui 230026, China

^d Sustainable Energy and Environmental Materials Innovation Center, Suzhou Institute for Advanced Research, University of Science and Technology of China, Suzhou, Jiangsu 215123, China

ARTICLE INFO

Keywords:

Three-in-one photosynthetic system
Covalent organic frameworks
Dual S-scheme heterojunction
Diluted CO₂ reduction
Syngas production

ABSTRACT

It remains a challenge to achieve overall photocatalytic conversion of CO₂ with H₂O into tunable syngas and O₂. Herein, by inserting BiVO₄ into the heterointerface of hollow core-shell CdS@T-COF S-scheme photocatalyst, an innovative CdS/BiVO₄@T-COF dual S-scheme heterojunction is developed, which gives an almost stoichiometric evolution of syngas (453.6 μmol g_{cat}⁻¹ h⁻¹) and O₂ (230.5 μmol g_{cat}⁻¹ h⁻¹). Moreover, the CO output and selectivity only decline by around 20% when pure CO₂ is replaced by diluted CO₂ (15%) atmosphere. The BiVO₄ embedding not only augments the internal electric field and band bending, upgrading the separation efficiency of active carriers, but also alters the roles of the components involved, separating the occurrence of CO, O₂ and H₂ evolution on T-COF, BiVO₄ and CdS in lower energy barriers. Besides, varying the T-COF thickness can modulate the availability of CO₂, H₂O and photon to different sites, thereby adjusting the CO/H₂ ratio in a wide window. This work opens an avenue for customizing three-in-one artificial photosynthetic systems for coupling three half reactions.

1. Introduction

Solar-driven catalytic transformation of CO₂ with H₂O into value-added and renewable fuels or chemical feedstocks, mimicking the natural photosynthesis, is an intriguing strategy to tackle the global warming and energy-supply crisis [1–3]. Nonetheless, undesirable charge recombination, insufficient light absorption and limited redox potentials of single-component semiconductor photocatalysts obstruct the solar-to-chemical energy conversion efficiency [4]. Besides, due to low CO₂ affinity of semiconductor surface and the lack of well-defined reactive sites, sluggish CO₂ reduction kinetics and uncontrollable reaction pathways also give rise to unsatisfactory photocatalytic activity and product selectivity, especially in low-concentration CO₂ conditions [5]. Cooperative coupling of inorganic semiconductors with covalent

organic frameworks (COFs) materials represents a feasible approach to resolve above dilemma [6–10]. Firstly, COFs generally possess visible-light-harvesting ability, which broaden the light harvesting range of as-formed organic-inorganic composites. Secondly, built-in-electric fields involved in the semiconductor/COF heterojunctions drive the spatial separation of photogenerated electrons and holes in different components. Thirdly, periodic pore structure and large surface area of COFs endow the as-formed hybrid photocatalysts with high CO₂ adsorption, enrichment, and activation abilities.

Designing a heterostructured photocatalyst with a suitable energy band structure and reasonable charge transfer model is essential for elevating the CO₂ photoreduction performance [11]. Among various types of heterojunctions, step-scheme (S-scheme) heterojunction is the optimal candidate for overall photoredox reactions because of its

* Corresponding author.

E-mail address: songbai@zjnu.edu.cn (S. Bai).

<https://doi.org/10.1016/j.apcatb.2024.123979>

Received 26 January 2024; Received in revised form 13 March 2024; Accepted 17 March 2024

Available online 18 March 2024

0926-3373/© 2024 Elsevier B.V. All rights reserved.

advantages in synchronously expediting the charge separation and maximizing the redox powers [12–14]. A typical S-scheme heterojunction is generally composed of a reduction photocatalyst (RP) and an oxidation photocatalyst (OP) with a staggered band alignment. Resulted from the Fermi level (E_f) difference between RP and OP, band bending (BB) occurs at the RP-OP interface together with the formation of an internal electric field (IEF), which jointly drives the interfacial transfer of conduction band (CB) electrons of OP and their recombination with valence band (VB) holes of RP in low redox abilities. Consequently, RP electrons and OP holes with high redox capabilities are separated for catalytic reactions. Despite S-scheme heterojunctions have witnessed enormous potential in boosting the CO₂ photofixation, whose CO₂ conversion efficiencies are still far from practical applications [15]. One major bottleneck is the inappropriate band alignment between RP and OP. In some cases, energy band mismatch results in undesirable charge transfer direction and the occurrence of redox reactions on the wrong locations [16]. Namely, OP is a more preferable photocatalyst for CO₂ reduction, while RP is a more suitable photocatalyst for H₂O oxidation, making it difficult to make full use of their advantages in advancing the photoredox catalysis. In other cases, in spite of the matched energy band alignment, the E_f difference between RP and OP is small, resulting in mild BB, weak IFE and thus low interfacial charge transfer efficiency [17]. In this circumstance, inadequate S-scheme recombination of useless carriers inevitably increase the probability of their recombination with useful ones. Besides, owing to the selection of inappropriate OP with improper VB position, sluggish H₂O oxidation kinetics also attenuate the CO₂ upgrading efficiency of S-scheme heterojunction [18]. Therefore, developing novel heterojunctions beyond S-scheme ones to overcome above shortcomings is highly desired.

Syngas, a mixture of CO and H₂, is one of the most important feedstocks for the production of many valuable chemicals and fuels via established industrial processes, such as Fischer-Tropsch synthesis, methanol synthesis and syngas fermentation [19,20]. Diverse CO/H₂ ratios of syngas are required for different downstream applications. Although great efforts have been devoted to exploring photocatalysts for syngas production, it is still a great challenge to precisely control the CO:H₂ ratio through the combination of photocatalytic CO₂ reduction and water splitting. Generally, simultaneous kinetics regulation of the two reactions emphasizes the necessity of accurately altering the surface fine structure of a photocatalyst and elaborately modulating the local electronic structure of the reactive sites, which is a complicated and challenging task [21,22]. Conversely, if two photocatalysts separately participate in the CO₂-to-CO and H₂O-to-H₂ conversion, this task would be simplified since it is much easier to adjust and control a single reaction pathway on the catalyst surface.

With the above in mind, in this contribution, we demonstrate a facile and versatile strategy to optimize the band alignment of semiconductor/COF heterojunction and boost the photocatalytic generation of syngas with tunable CO:H₂ ratios by transforming the single-junction S-scheme structure into double S-scheme one. Taking hollow CdS and T-COF as a proof-of-concept semiconductor and COF model, respectively, a CdS@T-COF (CT) core-shell S-scheme heterojunction is fabricated, which suffers from poor activity and low selectivity in CO₂ photoreduction because CdS instead of T-COF functions as an RP, dominantly accelerating the proton reduction reaction. Moreover, slow H₂O oxidation kinetics of T-COF eventuate in mismatched O₂ evolution. Meanwhile, the small E_f difference between CdS and T-COF abates the transfer and recombination of useless carriers. This issue can be circumvented by embedding BiVO₄, a typical H₂O oxidation semiconductor with a distinctly larger work function, into the heterointerface between them to form a dual S-scheme heterojunction, wherein the role of T-COF shell is turned from OP to RP, exerting its advantages in CO₂ enrichment and transformation. Additionally, newly introduced BiVO₄ enlarges the E_f difference between the components, thereby augmenting the IEF and BB involved for accelerated separation of useful charges. Further experimental and theoretical studies disclose that CdS, BiVO₄ and T-COF separately work

as H₂ evolution, H₂O oxidation and CO₂ reduction catalysts in the as-designed CdS/BiVO₄@T-COF (CBT), substantially reducing the rate-limiting barriers for H₂O-to-O₂ and CO₂-to-CO conversion when compared with CT. Benefiting from the simultaneous amelioration of charge kinetics and surface reactivity, optimized CBT achieves a superb syngas evolution rate of 453.6 $\mu\text{mol g}_{\text{cat}}^{-1} \text{h}^{-1}$ under visible light irradiation and an apparent quantum yield of 1.1% at 420 nm, along with a nearly stoichiometric evolution rate of O₂. Besides, T-COF shell also acts as a CO₂ enrichment component, and around 80% CO yield and selectivity of CBT maintain under diluted CO₂ atmosphere when compared with those in pure CO₂. More impressively, the availability of CO₂ and H₂O molecules to the T-COF, CdS and BiVO₄ sites together with the photon utilization efficiency of them can be regulated by adjusting the T-COF thickness of CBT. On this ground, the CO:H₂ ratios can be readily tuned in a wide window from 1:4.0–3.6:1. This work provides a new design strategy for the construction of artificial photosynthetic systems in efficient conversion of CO₂ and H₂O to syngas with controllable CO/H₂ ratio.

2. Experimental section

2.1. Preparation of hollow CdS nanospheres

In a typical synthesis [23], SiO₂ spheres were firstly prepared as a template by the Stöber method. 1.5 mL of ammonia (NH₃·H₂O, 28%) was added dropwise into a 33 mL mixture of ethanol and water (2:1, v/v) and stirred for 5 min at 30 °C in an oil bath. Next, 5 mL of TEOS was dropped into the mixture, which was stirred at 30 °C for 0.5 h. The resulting SiO₂ nanospheres were washed with ethanol and water alternately for three times, and dried at 60 °C in an oven overnight.

SiO₂@CdS was then synthesized with SiO₂ spheres as precursors. Firstly, 150 mg of as-obtained SiO₂ spheres were dispersed in 100 mL of water under ultrasound assistance. Then, 1 mL of 1 M sodium citrate aqueous solution was added into the above solution and kept stirring 10 min. Next, 0.5 mL of 1 M CdCl₂ aqueous solution was added into the mixture dropwise. After stirring for additional 20 min, 2 mL of ammonia (NH₃·H₂O, 28%) and 2 mL of 1 M thiourea aqueous solution were slowly added sequentially. Finally, the well-distributed solution was transferred and heated in an oil bath at 80 °C for 3 h. After natural cooling, the yellow precipitate was centrifuged and washed with water and ethanol to remove the impurities, and dried in a vacuum at 60 °C overnight. The obtained powder was then put into 50 mL of 1 M sodium hydroxide aqueous solution and etched at 90 °C for 3 h to remove the SiO₂ template. After the reaction finished, the resulting yellow products were collected and washed with ethanol, the sediment was dried in a vacuum drying oven at 60 °C for 12 h.

2.2. Preparation of BiVO₄ nanoparticles

In a typical procedure for the synthesis of BiVO₄ nanoparticles, 0.4851 g of bismuth nitrate was dissolved in 10 mL of acetic acid with vigorous stirring at room temperature. Then it was mixed with 40 mL of ethanol containing 0.2652 g of VO(acac)₂. Next, 10 g of PVP was added to the mixture and stirred vigorously until a homogeneous solution was achieved. The solution was transformed into a 100 mL round-bottom flask and refluxed under magnetic stirring at 80 °C for 2 h. After cooling to room temperature, the yellow precipitate was collected by centrifugation and washed with anhydrous ethanol several times. The yellow product was ultimately dried at 40 °C in a vacuum oven, and heated in a furnace at 400 °C for 2 h.

2.3. Preparation of T-COF

In a typical synthesis of T-COF [16], 14.2 mg of 2,4,6-tris(4-aminophenyl)-1,3,5-triazine, 6.5 mg of 1,3,5-benzenetricarboxaldehyde and 5 mL of acetonitrile were added in a glass vial. After 30 min

ultrasonication treatment, 0.4 mL of 12 M acetic acid was added to the reaction system. Then the glass vial was sealed and kept at room temperature for 96 h without stirring. The product was separated, washed with N,N-dimethylformamide and water, and finally dried in a vacuum oven at 70 °C for 12 h to obtain yellow solid.

2.4. Preparation of CBT and CT

Firstly, 19.4 mg of BiVO₄ was dispersed in 5 mL of ethanol, which was added drop by drop to 50 mL of ethanol containing 18 mg of CdS. After ultrasonication for 10 min, CdS/BiVO₄ (CB) precursor was obtained through centrifugation, washed with ethanol several times and dried at 60 °C in a vacuum overnight. Subsequently, the as-prepared CB and 14.2 mg of 2,4,6-tris(4-aminophenyl)-1,3,5-triazine were mixed with 3 mL acetonitrile in a glass vial. After 60 min of ultrasonication, 6.5 mg of 1,3,5-benzenetricarboxaldehyde and 2 mL of acetonitrile were added to the vial. After ultrasonication treatment for another 30 min, 0.4 mL of 12 M acetic acid was added into the solution. Then the vial was sealed and kept at room temperature for 96 h without stirring. The obtained product was filtered, washed with N,N-dimethylformamide and water, and finally dried in a vacuum oven at 70 °C for 12 h. For the synthesis of CBT with other loading amounts of BiVO₄, 6.5, 13.0, 25.9 and 32.4 mg of BiVO₄ was used, respectively. As for the synthesis of CBT with other T-COF thicknesses, 13.5, 15, 16.5 and 19.5 mg of CB was used, respectively. CT was prepared by following the same synthetic process as CBT except for the use of 18 mg CdS instead of CB as a precursor.

2.5. Photocatalytic CO₂ reduction measurements

To investigate the photocatalytic performance of the samples in CO₂ reduction, 5 mg of photocatalysts were placed in a quartz dish at the bottom of a 150 mL photocatalytic reactor (Beijing Perfectlight, China). 300 μL H₂O and 500 μL acetonitrile were injected at the same time which were ensured not touch the catalysts. Prior to the test, high-purity CO₂ (99.999%) or CO₂/Ar mixed gas (v/v = 15:85) was bubbled into the system for at least 30 min to reach CO₂ adsorption-desorption balance. Subsequently, the light-irradiation experiment was performed by using a 300 W Xe lamp (PLS-SXE300D/300DUV, Beijing Perfectlight, China) with visible light as the illumination source, which was realized using both a 420-nm cutoff filter (long-wave-pass) and a 780-nm cutoff filter (short-wave-pass). The power density of incident light was measured to be 100 mW cm⁻² using a radiometer (FZ-A, China). The photocatalytic reaction was performed for 4 h. The gaseous mixture was analyzed using a gas chromatograph (GC-2014, Shimadzu) with Ar as the carrier gas. The amounts of H₂ and O₂ were determined using a thermal conductivity detector (TCD). CO was converted to CH₄ by a methanation reactor and then analyzed by a flame ionization detector (FID). Besides, other possible products were also detected. For instance, CH₄ was measured by a FID of gas chromatography (GC-2014, Shimadzu). CH₃OH was analyzed using a FID of gas chromatography (Agilent 8860). HCOOH was analyzed using a ¹H nuclear magnetic resonance (¹H NMR) spectrometer (Bruker Avance 600 MHz). H₂O₂ was detected by UV-vis absorption spectroscopy using o-tolidine as an indicator. During the stability test, the used photocatalysts were collected after each run by centrifugation, washed with water, and dried in a vacuum, which were then re-dispersed in the reactor for the next round of recycling experiment. Isotope-labeling experiments were performed using ¹³CO₂ instead of ¹²CO₂, and the products were analyzed using gas chromatography-mass spectrometry (7890B/5977 A, Agilent). H₂ and CO selectivity were calculated according to the average evolution rates of the reduction products as well as the electrons required to generate the products using the following equation:

$$\text{H}_2 \text{ selectivity} = 2v(\text{H}_2)/[2v(\text{CO}) + 2v(\text{H}_2)] \times 100\% \quad (1)$$

$$\text{CO selectivity} = 2v(\text{CO})/[2v(\text{CO}) + 2v(\text{H}_2)] \times 100\% \quad (2)$$

3. Results and discussion

3.1. Sample synthesis and characterization

The synthetic procedure of CBT is illustrated in Fig. 1a. Hollow CdS nanospheres with an average thickness of 34.5 nm and diameter of 740.4 nm were firstly synthesized with the assistance of silica template (step i and ii, Fig. S1 and S2) [23]. Afterwards, positively charged BiVO₄ nanoparticles with an average size of 154.1 nm were pre-synthesized (Fig. S3) and deposited on the outer surface of negatively charged CdS spheres through electrostatic interaction (step iii) (Fig. S4). Transmission electron microscopy (TEM) images indicate that the loading of BiVO₄ does not affect the morphology of CdS (Fig. 1b₁,b₂). The as-obtained CB was then coated with T-COF by the condensation of 1,3,5-benzenetricarboxaldehyde and 2,4,6-tris(4-aminophenyl)-1,3,5-triazine (step iv). As shown in Fig. 1c₁ and c₂, both CdS and BiVO₄ are uniformly covered by T-COF shell, forming ternary CBT with BiVO₄ sandwiched between CdS and T-COF. Scanning TEM (STEM) and corresponding energy-dispersive X-ray spectroscopy (EDS) elemental mapping reveal the even distribution of Cd and S elements in the inner hollow core, Bi, V and O elements in the middle component, and C, N and O elements in the outer shell (Fig. 1c₄). According to high-resolution TEM (HRTEM) images (Fig. 1b₃ and c₃), clear lattice fringes with D-spacings of 3.6 and 3.1 Å can be observed on the supporting and anchoring component of CB, corresponding to (100) crystal plane of CdS and (112) plane of BiVO₄, respectively. The further T-COF coating obscures the lattice fringes of CBT. The reason is that T-COF loses crystallinity upon exposure to electron beam irradiation. Previous reports attribute this phenomenon to the disruption of the weak π-π interactions between adjacent COF layers [24,25]. Besides, by tuning the dosage of BiVO₄ and CB precursor in step iii and iv procedure, the loading amount of BiVO₄ and thickness of T-COF in CBT can be facily regulated, respectively (Table S1 and Fig. S5). As reference samples, pure T-COF and CT were prepared by following the step iv procedure as CBT except the absence of CB precursor and the use of hollow CdS instead of CB as a precursor, respectively (Fig. S6 and Fig. 1d). For ease of comparison, the average T-COF thickness of CT is kept close to that of CBT during the following spectroscopic characterizations.

The structures of as-synthesized samples were investigated by powder X-ray diffraction (XRD). As shown in Fig. 2a, CdS and BiVO₄ exhibit typical peaks assigned to hexagonal phase CdS (JCPDS no. 80-0006) and monoclinic phase BiVO₄ (JCPDS no. 75-1867), respectively. As for T-COF, all peaks are in agreement with the simulated AA stacking mode. Both CdS and T-COF peaks can be observed in the pattern of CT, while additional characteristic peaks of BiVO₄ appear in that of CBT. UV-vis diffuse reflectance spectroscopy shows that bare CdS, BiVO₄ and T-COF exhibit intrinsic optical absorption band in visible region (Fig. 2b). Based on the derived Tauc plots, their bandgap energies are determined to be 2.31, 2.47 and 2.75 eV, respectively (Fig. S7). As for CT and CBT, the absorption spectrum is a simple superposition of that of the components involved. According to the N₂ sorption measurements, the Brunauer-Emmett-Teller (BET) specific surface areas of CdS, BiVO₄, T-COF, CT and CBT are 63.9, 19.0, 602.6, 663.5 and 410.6 m² g⁻¹, respectively, demonstrating that porous T-COF accounts for the high specific surface area of CT and CBT (Fig. 2c). The highest BET area of CT highlights the cooperation of T-COF and hollow CdS in accelerating the mass transport, while the relatively smaller BET area of CBT should be ascribed to mass contribution of BiVO₄.

The chemical states of surface elements were disclosed by X-ray photoelectron spectra (XPS). High-resolution Cd3d spectra show Cd3d_{3/2}/Cd3d_{5/2} doublet peaks of CdS, and the corresponding binding energies shift to higher values after the co-loading of BiVO₄ and T-COF (Fig. 2d).

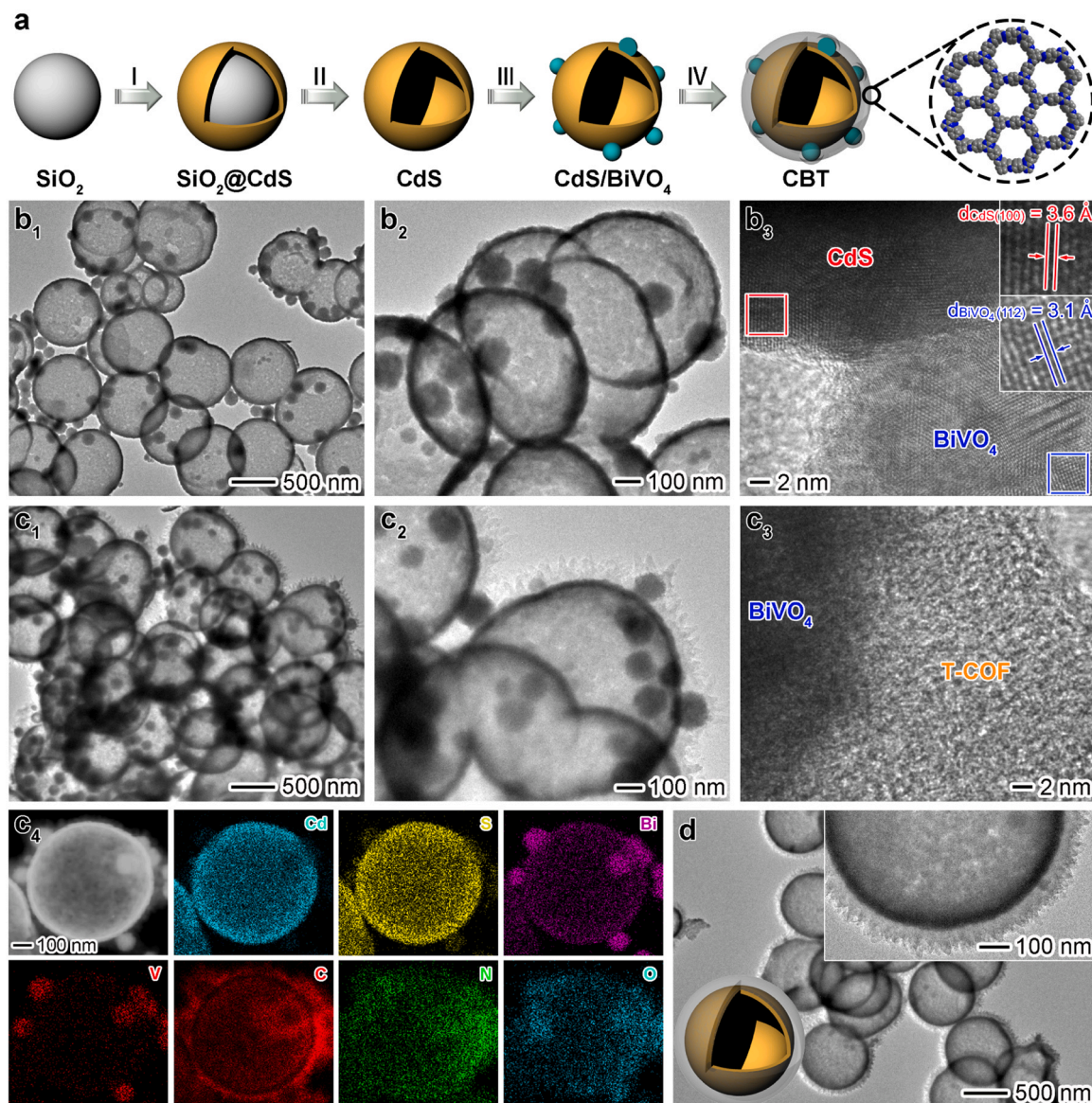


Fig. 1. Synthesis and electronic microscopy characterizations of CBT and reference samples: (a) schematic illustrating the synthetic procedure of CBT; (b₁, b₂) TEM and (b₃) HRTEM images of CB; (c₁, c₂) TEM, (c₃) HRTEM, (c₄) STEM images and corresponding EDS-mapping profiles of CBT; (d) TEM images of CT.

Similar positive shift of S2p_{1/2}/S2p_{3/2} peaks is observed in the S2p spectra, which is overlapped with Bi4f spectra in Fig. 2e. In sharp contrast, Bi4f_{5/2}/Bi4f_{7/2} doublet peaks of CBT move to lower binding energies when compared with bare BiVO₄. Besides, N1s binding energy of CBT displays a positive shift in comparison with that of pristine T-COF (Fig. 2f). The XPS results indicate the movement of free electrons from CdS and T-COF to BiVO₄ when they come into contact [26]. When in situ irradiated XPS was performed on CBT, Cd3d_{3/2}/Cd3d_{5/2}, S2p_{1/2}/S2p_{3/2} and N1s peaks shift negatively by 0.18, 0.19 and 0.18 eV compared to those in the dark, while Bi4f_{5/2}/Bi4f_{7/2} peaks undergo a positive shift of 0.11 eV, manifesting the inverse flow of photogenerated electrons from BiVO₄ to CdS and T-COF under light illumination (Fig. 2d-f) [27]. Similar first positive and then negative shifts in the binding energies of Cd3d and S2p peaks are observed in the XPS spectra of CT with CdS as a reference sample and under light irradiation, respectively (Fig. S8). Notably, the N1s binding energy of CT is contrary to the previous moving direction of CBT, which displays a negative and positive shift relative to that of pure T-COF and under light illumination, respectively. These results demonstrate the transmission of free electrons from CdS to T-COF upon their contact and the migration of photoelectrons in the

opposite direction. Moreover, the shift degree of CT in the binding energies is not as prominent as that of CBT, indicative of relatively lower charge transfer efficiencies under dark and light conditions.

3.2. Photocatalytic performances analysis

Photocatalytic CO₂ reduction reactions were performed in water/acetonitrile mixture under visible light irradiation. Acetonitrile was selected because of its high CO₂ solubility [28]. When CBT was used as a catalyst, CO and H₂ were detected as the reduction products and O₂ was generated as the product of H₂O oxidation half reaction (Fig. 3a). No other gaseous or liquid product was detected for CBT and reference samples. The H₂ output of CBT decreases monotonically with the increasing T-COF thickness from 54.4 to 275.7 nm, while the CO yield exhibits a volcano-shaped trend with the highest CO evolution rate achieved by CBT with an average T-COF thickness of 114.0 nm (Fig. 3b). Moreover, CO selectivity gradually raises as the T-COF thickness increases, allowing the tunable CO: H₂ molar ratio from 1:4.0–3.6:1. According to the numbers of electrons involved (2 H⁺ + 2e⁻ → H₂; CO₂ + 2 H⁺ + 2e⁻ → CO + H₂O), the highest electron consumption rates were

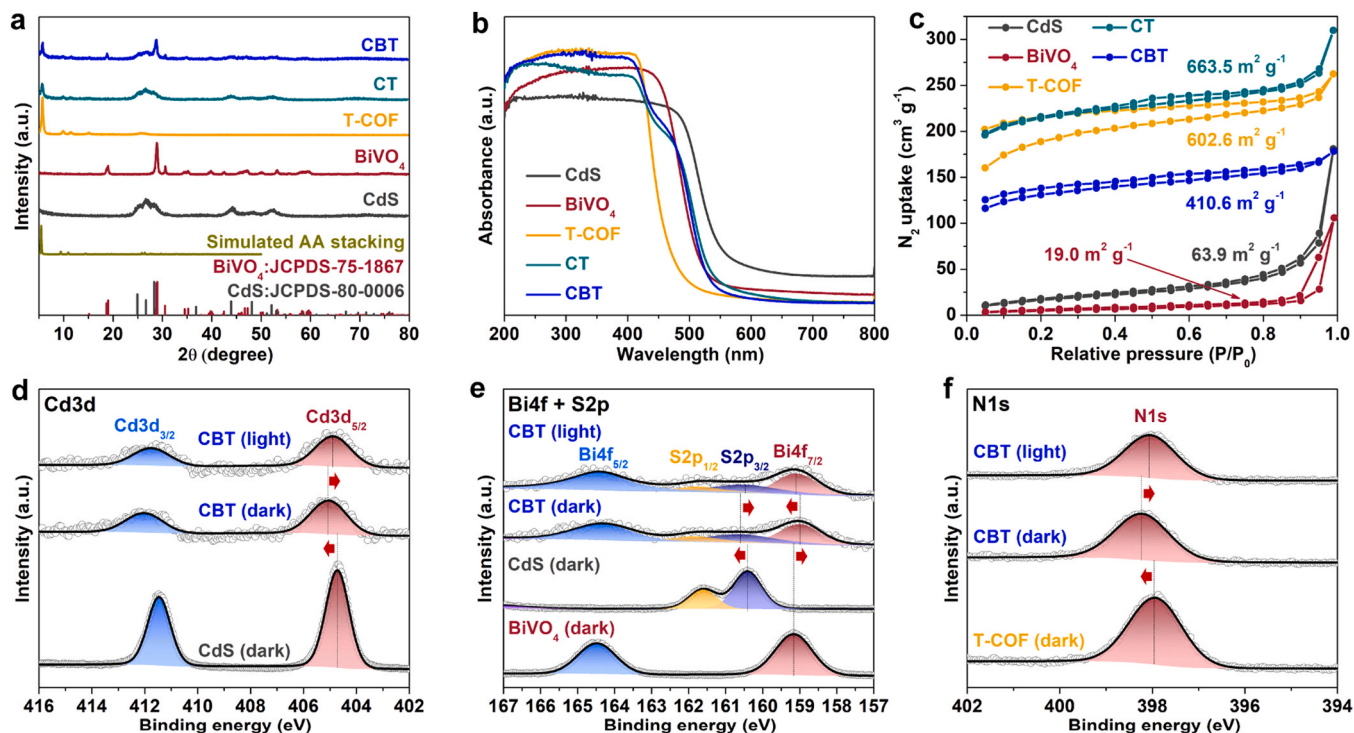


Fig. 2. Spectroscopic characterizations of CBT and reference samples: (a) XRD patterns; (b) UV-vis diffuse reflectance spectra; (c) N_2 sorption isotherms; (d-f) high-resolution XPS spectra: (d) Cd3d, (e) Bi4f + S2p and (f) N1s.

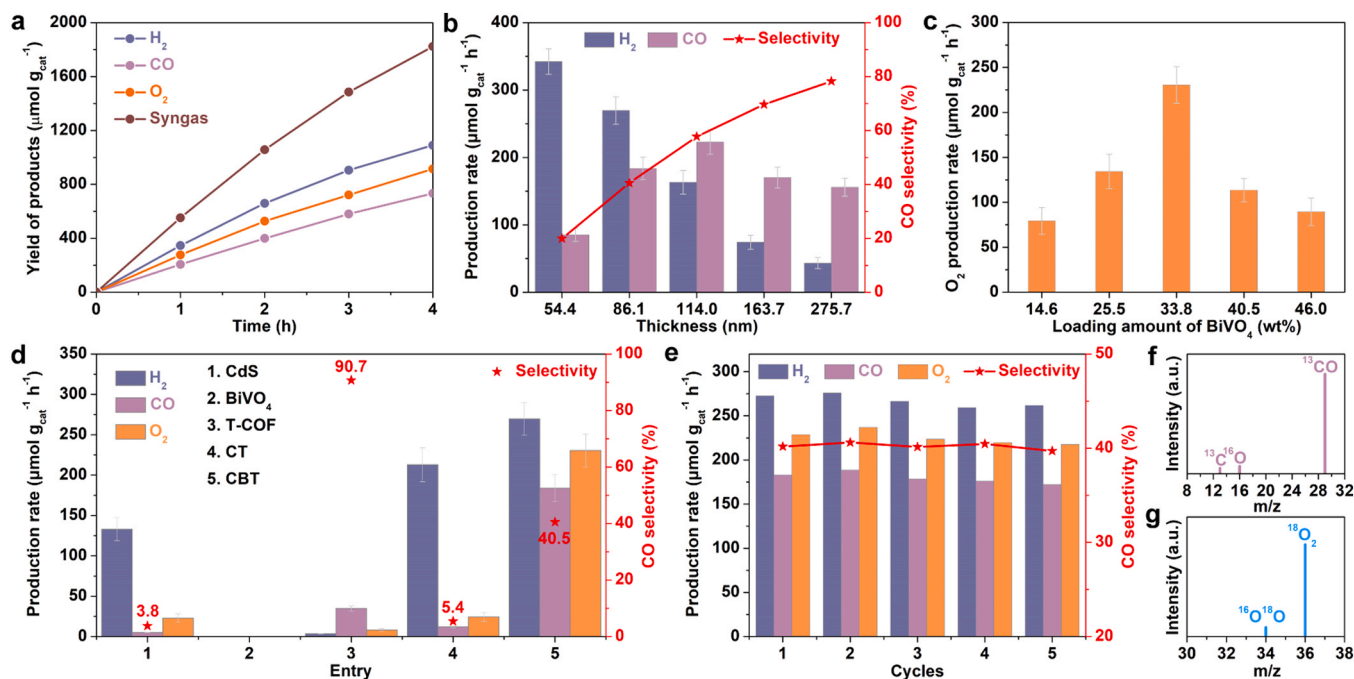


Fig. 3. Photocatalytic performance of CBT and reference samples: (a) yields of H_2 , CO , O_2 and syngas over CBT (86.1 nm T-COF thickness, 33.8 wt% $BiVO_4$) as a function of reaction time; (b) CO_2 reduction activities and CO selectivities over CBT with different T-COF thicknesses; (c) O_2 evolution rates of CBT with various loading amounts of $BiVO_4$; (d) comparative activities and selectivities of optimized CBT with reference samples; (e) stability tests over optimized CBT; (f, g) mass spectrum of the generated (f) ^{13}CO and (g) $^{18}O_2$.

achieved by CBT with 86.1 nm T-COF thickness, suggesting the maximal charge utilization occurs at moderate T-COF coverage (Fig. S9). With optimized T-COF thickness, Fig. 3c also exhibits a volcano-type relationship between the O_2 generation rate and the loading amount of $BiVO_4$. The decline in the syngas and O_2 output when the thickness of

T-COF and loading weight of $BiVO_4$ exceeds a certain value is mainly resulted from their light shielding effect on CdS core. It is worth noting that the CO selectivity of CBT is nearly unchanged by tuning the $BiVO_4$ amount, suggesting that $BiVO_4$ is a critical component for oxidation half reaction instead of reduction half reaction (Fig. S10).

With the optimal BiVO₄ content of 33.8 wt% and T-COF thickness of 86.1 nm, the photocatalytic activity of CBT was compared with those of reference samples in Fig. 3d. Bare CdS and T-COF exhibit H₂ and CO as the primary reduction product, respectively, and the corresponding CO selectivity is 3.8% and 90.7%, in accordance with previous reports [29, 30]. Conversely, BiVO₄ produces neither H₂ nor CO since its CB level is not negative enough to reduce H₂O and CO₂. With the combination of the three components, an optimized H₂ evolution rate of 269.8 $\mu\text{mol g}_{\text{cat}}^{-1} \text{h}^{-1}$ and CO evolution rate of 183.8 $\mu\text{mol g}_{\text{cat}}^{-1} \text{h}^{-1}$ are achieved by CBT, which are around 2.0 and 35.0 times higher than those of CdS, and nearly 75.2 and 5.3 folds higher than those of T-COF. The corresponding apparent quantum efficiency (AQE) for syngas production reaches up to 1.1% at 420 nm, surpassing previous reports under comparable conditions (Table S2). Contrastingly, CT with an approximate T-COF thickness affords a dominant H₂ production with a rate of 212.9 $\mu\text{mol g}_{\text{cat}}^{-1} \text{h}^{-1}$ and a selectivity of 94.6% together with a trace amount of CO evolution (12.2 $\mu\text{mol g}_{\text{cat}}^{-1} \text{h}^{-1}$), whose syngas productivity (225.1 $\mu\text{mol g}_{\text{cat}}^{-1} \text{h}^{-1}$) is far less than that of CBT (453.6 $\mu\text{mol g}_{\text{cat}}^{-1} \text{h}^{-1}$). These comparisons prove that BiVO₄ introduction accounts for superb CO generation and superior syngas production of CBT. In terms of oxidation half reaction, CBT delivers an average O₂ evolution rate of 230.5 $\mu\text{mol g}_{\text{cat}}^{-1} \text{h}^{-1}$, 10.1, 27.5 and 9.5 times those of CdS, T-COF and CT, highlighting the critical role of BiVO₄ in boosting H₂O oxidation. Impressively, the molar ratio of O₂ to syngas over CBT is calculated to be 1.00:1.97, matching well with the stoichiometric redox reactions (Fig. S11). As for other samples, the ratio is far below the theoretical value owing to delayed H₂O oxidation process. Additionally, low-concentration CO₂ photoreduction was further carried out by replacing pure CO₂ with 15% CO₂/Ar as gas source. As shown in Fig. S12, a CO evolution amount of 146.6 $\mu\text{mol g}_{\text{cat}}^{-1} \text{h}^{-1}$ and selectivity of 32.6% was detected for CBT, merely declines by 20.3% and 19.5% when compared with those in pure CO₂ atmosphere, respectively, while only H₂ was produced by pristine CdS and CB. This result underscores the pivotal role of T-COF shell in capturing low-concentration CO₂ and creating an enriched CO₂ atmosphere for reduction half reaction. The CO₂ uptake of T-COF is as high as 31.1 cm³ g⁻¹ under 1 atm, ca. 7.0 times higher than that of hollow CdS (Fig. S13).

To evaluate the stability of CBT, cyclic tests were performed for five successive cycles lasting up to 20 h. With stabilized CO selectivity in the range of 39.7–40.5%, no visible decrease in the photoactivity is observed (Fig. 3e). Moreover, there is no observable change in the structure, morphology and composition of the used CBT when compared with the fresh one (Fig. S14–S16). The above results jointly support the excellent recyclability and reusability of the ternary photocatalyst. We also tested the stability of CBT in electrocatalytic O₂ evolution, in which only a slight current drop occurs in the polarization curves after running 2000 continuous cycles, proving the good stability of CBT in the electrolyte (0.5 M KOH) (Fig. S17). Since T-COF and acetonitrile also contain C element, to validate the carbon source of the generated CO, control experiments have been performed, and no carbon-containing product can be detected without catalyst, CO₂ or light irradiation. Besides, ¹³CO₂ isotopic experiment was carried out, and the GC-MS peaks at *m/z* = 29, 16 and 13 can be indexed to ¹³CO and its fragments (Fig. 3f) [31]. These results collectively validate that the produced CO entirely comes from CO₂ photofixation. When H₂O was replaced by H₂¹⁸O as a reactant, a main ¹⁸O₂ peak at *m/z* = 36 was detected together with a weak ¹⁶O¹⁸O peak at *m/z* = 34, confirming that the generated O₂ is mainly derived from H₂¹⁸O oxidation (Fig. 3g). The small amount of ¹⁶O content originates from H₂¹⁶O produced during the conversion of C¹⁶O₂ into C¹⁶O. No peak at *m/z* = 32 appears, excluding the possibility of direct transformation of C¹⁶O₂ to ¹⁶O₂ (CO₂ → CO + 1/2 O₂). Therefore, all generated O₂ comes from H₂O oxidation.

3.3. Charge transfer/separation kinetics analysis

To further uncover the underlying reasons for the photocatalytic enhancements, photoluminescence (PL) and photoelectrochemical

(PEC) measurements were employed to assess the separation and transfer behaviors of photogenerated carriers. Fig. 4a shows that CT exhibits a relatively lower PL peak intensity in comparison with CdS and T-COF, suggesting the suppression of radiative charge recombination. With the incorporation of BiVO₄, PL quenching degree is upgraded, indicative of the further improved charge separation in CBT. Similarly, transient photocurrent density of CT under chopped visible light irradiation is higher than those of CdS and T-COF but lower than that of CBT (Fig. 4b). Meanwhile, as revealed by the electrochemical impedance spectroscopy (EIS), the Nyquist arc radius decreases in the sequence: T-COF < CdS < BiVO₄ < CT < CBT, following the same order as photocurrent enhancement, which infers that the improved charge separation efficiency is accompanied with reduced charge-transfer resistance (Fig. 4c). The PEC results corroborate that the coupling of BiVO₄ with CdS and T-COF expedites the transfer and separation of photocreated carriers, thus contributing to considerably elevated photoactivity of CBT.

To in-depth explore the intrinsic role of BiVO₄ in ameliorating the charge kinetics, energy band structures of the components involved in CT and CBT were determined by ultraviolet photoelectron spectroscopy (UPS) (Fig. S18). According to the secondary cutoff energy in the high binding energy region, the E_f levels of CdS, BiVO₄ and T-COF are located at -0.47, 1.03 and -0.17 V vs. NHE (pH = 0), respectively. Their valence band maximum (VBM)/highest occupied molecular orbital (HOMO) positions are then determined to be 1.38, 3.08 and 2.03 V vs. NHE, respectively, deriving from its energy difference with E_f reflected by the UPS in the low binding energy region. Furthermore, based on E_g (Fig. S7), the corresponding conduction band minimum (CBM)/lowest unoccupied molecular orbital (LUMO) positions are calculated to be -0.93, 0.61 and -0.72 V vs. NHE, respectively. Namely, the E_f, CBM/LUMO and VBM/HOMO levels of T-COF are lower than those of CdS but higher than those of BiVO₄. In view of the staggered band alignment between the components, the charge transfer directions were identified by electron spin resonance (ESR) technique using 5,5-dimethyl-1-pyrroline N-oxide (DMPO) as a free radical trapping agent (Fig. S19). It can be found that CdS and T-COF only produce DMPO-•O₂ signal under visible light illumination since their VBM/HOMO are not positive than the oxidation potential of H₂O/•OH (2.38 V vs. NHE), while BiVO₄ merely generates DMPO-•OH signal because its CBM is not negative than the reduction potential of O₂/•O₂ (-0.046 V vs. NHE). The behavior of CT is similar to its components. In contrast, both DMPO-•O₂ and DMPO-•OH signals are created by CBT, whose intensities are obviously higher than its counterparts, excluding the possibility of forming type-II heterojunction [32]. Otherwise, neither DMPO-•O₂ nor DMPO-•OH signal would appear when photoelectrons and holes respectively migrate to BiVO₄ with the lowest CBM and CdS with the highest VBM.

Based on above XPS and ESR results, a single and dual S-scheme charge transfer model is proposed for CT and CBT, respectively. As depicted in Fig. 4d, the hybridization between CdS and T-COF induces the spontaneous flow of free electrons from CdS to T-COF to reach an E_f equilibrium, giving rise to the construction of an IEF pointing from CdS to T-COF as well as upward and downward BB of CdS and T-COF, respectively. Resulted from the small E_f difference between CdS and T-COF, the CdS→T-COF electron flow is not obvious, causing weak IEF and mild BB, and accounting for slight XPS shift of CT relative to its components. Under visible light irradiation, the IEF and BB provide feeble driving force for the S-scheme transfer and recombination of pointless T-COF electrons and CdS holes, inadequately separating the pointful photoinduced electrons on the CB of CdS and holes on the HOMO of T-COF for redox reactions. When BiVO₄ is sandwiched between CdS and T-COF, since the E_f of BiVO₄ is significantly lower than those of CdS and T-COF, both CdS and T-COF donate free electrons to BiVO₄, leading to the formation of two IEFs in opposite directions together with the downward BB of BiVO₄ and upward BB of CdS and T-COF. Benefitting from their large E_f difference, apparent electron movement occurs, causing strong IEFs and severe BB. When CBT is exposed to illumination, the

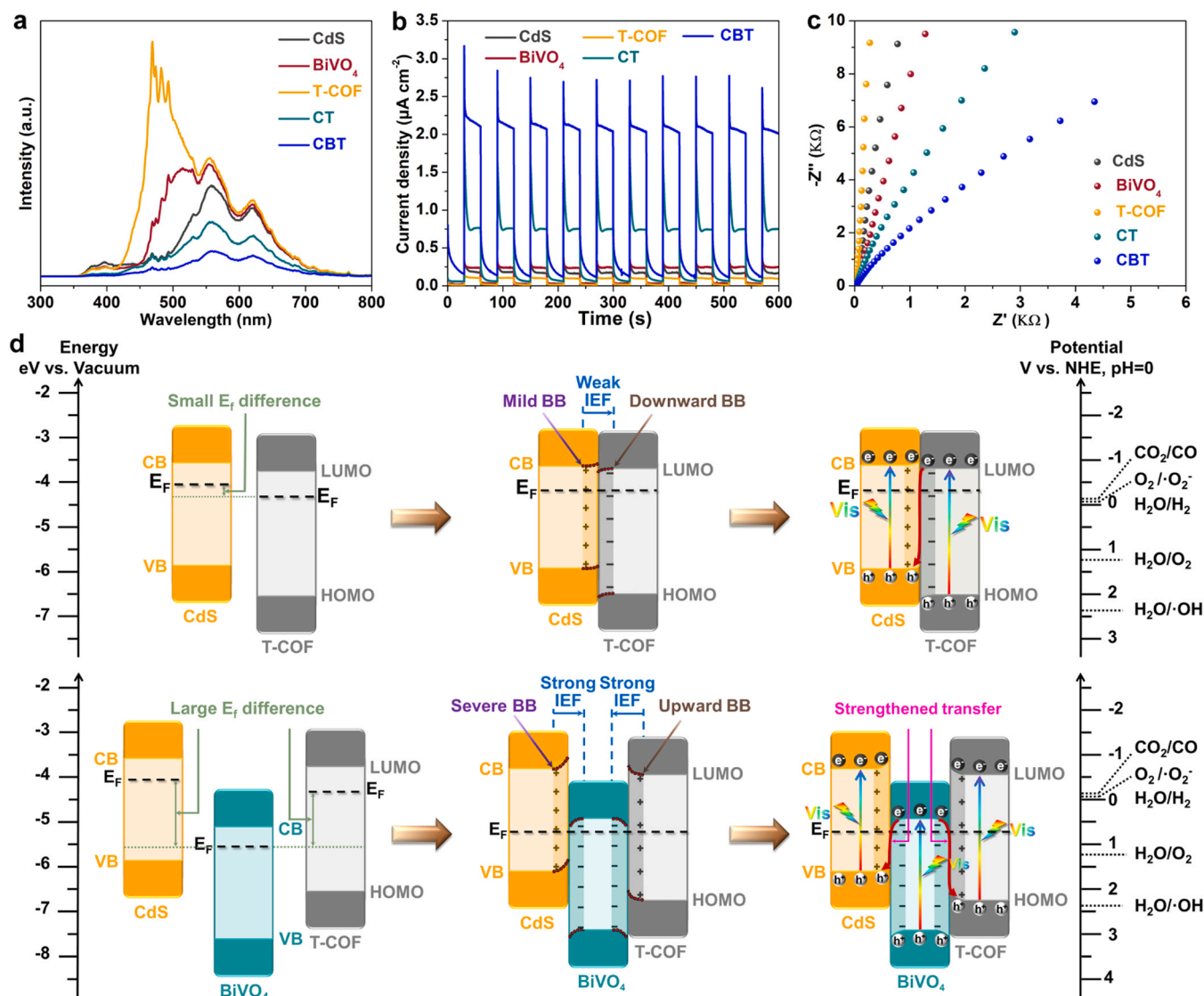


Fig. 4. Charge kinetics analysis of CBT and reference samples: (a) PL spectra; (b) transient photocurrent responses; (c) EIS Nyquist plots; (d) schematic illustrating the charge separation/transfer mechanisms in CT (top) and CBT (bottom).

amplified IEFs and BB strengthen the interfacial transportation of BiVO₄ electrons to consume the pointless holes of CdS and T-COF, enabling sufficient separation of meaningful holes on the VB of BiVO₄ and active electrons on the CB/LUMO of CdS and T-COF for photoredox catalysis. The improved charge transfer and separation efficiencies of CBT well explain the more pronounced shift in the XPS and its stronger DMPO-•O₂ signal in contrast to CT [33]. Enabled by the dual S-scheme charge transfer pathways, the more thorough recombination of weak carriers balances the separation of active holes of BiVO₄ and electrons of CdS and T-COF, which makes the reduction and oxidation half reaction stoichiometrically proceeds in the photocatalytic process.

In order to visualize the different S-scheme charge transfer pathways, photoirradiated Kelvin probe force microscopy (KPFM) was applied to probe the charge distribution in CT and CBT. Before light irradiation of CT, surface potential of CdS core is 60.60 mV higher than that of T-COF shell, indicating the existence of charge redistribution and the establishment of IEF directed from CdS to T-COF (Fig. 5a) [34]. Upon visible light irradiation, without distinct change in the atomic force microscopy image, surface potential at CdS and T-COF sites respectively experiences a slight decrease and increase, and the potential difference between them declines to 49.42 mV. The change of surface potential reveals the migration of photoelectrons from T-COF to CdS, again proving the

S-scheme charge transfer mechanism [35]. Distinct from CT, apart from CdS core, additional higher surface potential appears in the outermost shell of CBT, while lower surface potential is located in the middle region, implying the movement of free electrons from CdS and T-COF to the sandwiched BiVO₄ (Fig. 5b). Moreover, the surface potential difference between them is 80.15 mV in the dark, 1.3 times larger than that of CT, hinting the occurrence of more pronounced charge redistribution and the building-up of more prominent IEFs. Further light illumination remarkably raises the surface potential of BiVO₄ and lowers those of CdS and T-COF, reducing their potential difference to 36.90 mV. The more distinct change in the potential difference before and after illumination evidences the accelerated migration of photoelectrons from the former to the two latter components.

3.4. Surface reaction dynamics analysis

Aside from charge kinetics, the effect of BiVO₄ introduction on the surface reactivity of CBT was also deliberated. According to the aforementioned charge transfer mechanisms, inserted BiVO₄ turns the function of T-COF from OP to RP, and itself substitutes the OP role of T-COF. That is to say, relative to CT, CBT not only provides additional T-COF sites for reduction half reactions, but also shifts the oxidation sites from

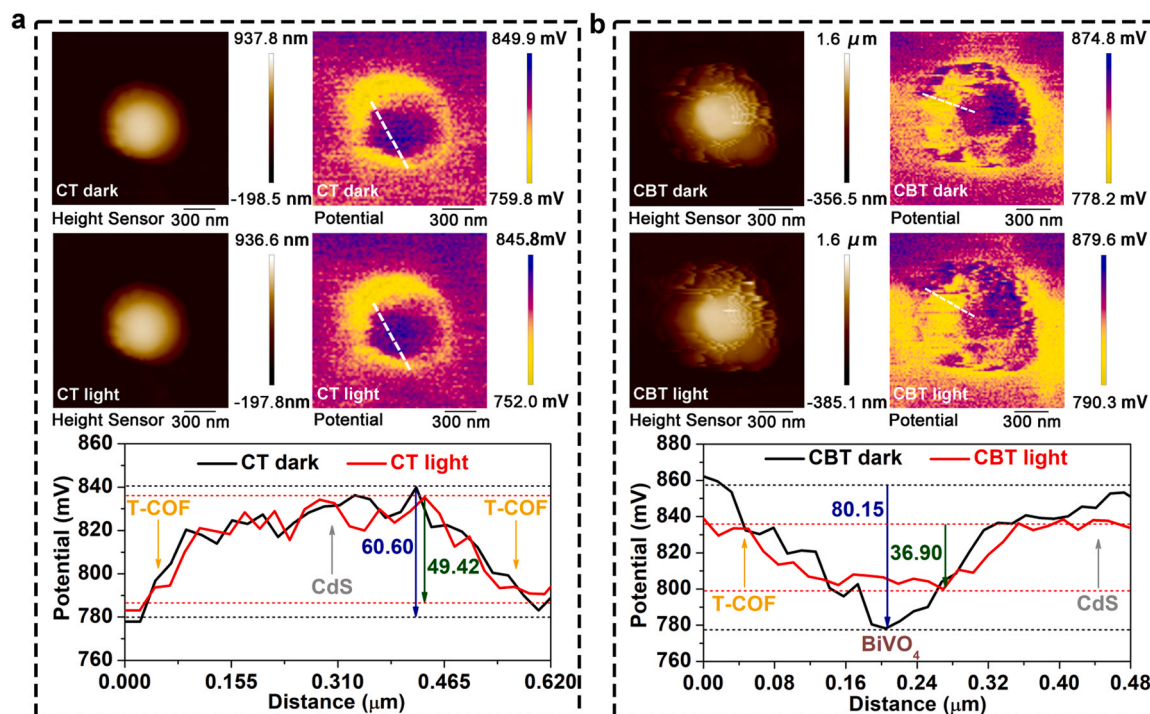


Fig. 5. Comparative KPFM studies of (a) CT and (b) CBT: AFM images (left) and the corresponding KPFM potential images (right) in darkness and under light illumination; (bottom) the line-scanning surface potential curves in darkness and under light illumination.

T-COF to BiVO_4 , which inevitably triggers the alteration of redox reactivities. To identify the contribution of T-COF to syngas evolution, CO_2 temperature-programmed desorption (CO_2 -TPD) measurements were conducted. As shown in Fig. 6a, CdS displays weak desorption peaks at around 105, 289 and 388 °C, while much stronger desorption peaks at higher temperatures (469, 562 and 671 °C) are clearly observed for T-COF, indicating the stronger interaction between CO_2 molecules and T-COF surface. It can be inferred that T-COF is a more promising candidate for CO_2 photoreduction in comparison with CdS. The reduction selectivities of CdS and T-COF were also unraveled by linear sweep voltammetry (LSV) measurements in Ar- and CO_2 -saturated KHCO_3 electrolyte, respectively (Fig. 6b). With regard to CdS, the reduction current density under Ar atmosphere is markedly higher than that under CO_2 atmosphere at the same voltage, implying that H_2 evolution is the predominant reaction on the CdS surface [36]. In contrast to CdS, the reduction current density of T-COF augments substantially with the replacement of Ar atmosphere by CO_2 atmosphere, demonstrating that the T-COF surface is more active in reducing CO_2 molecules relative to H_2O molecules [37].

To elaborate further on this point, density functional theory (DFT) calculations were performed (Fig. S20), and Gibbs free energy diagrams for CO_2 -to-CO reduction on CdS(001) and T-COF surface were compared in Fig. 6d. Clearly, the CO_2 adsorption energy on T-COF surface is more negative than that on CdS. Moreover, $^*\text{COOH}$ formation and $^*\text{CO}$ desorption are two endothermic steps for both cases. Nonetheless, the uphill energies of the two steps on T-COF surface are 0.56 and 0.51 eV, respectively, which are lower than those on CdS (0.67 and 0.71 eV), convincing that T-COF is more energetically feasible for CO_2 -to-CO transformation [38]. Besides, hydrogen adsorption Gibbs free energy (ΔG_{H^*}) was calculated to explore the proton reduction behaviors on the two surfaces (Fig. 6e). The adsorption of $^*\text{H}$ on CdS surface is an exothermic process, and the corresponding ΔG_{H^*} value is -0.20 eV. Contrastingly, $^*\text{H}$ adsorption on T-COF is thermodynamically unfavorable must overcome an energy barrier of $\Delta G_{\text{H}^*} = 0.42$ eV. The larger absolute value of ΔG_{H^*} undercores that T-COF is less practicable to achieve the equilibrium of hydrogen adsorption/desorption, not

favorable for H_2 evolution [39]. The above simulations unveil that CdS core and T-COF shell of CBT respectively catalyze the H_2 evolution and CO_2 reduction in lower reaction energy barriers, which is the main reason why CBT exhibits higher CO selectivity relative to CT. In the latter sample, only CdS partakes in the reduction half reaction, causing highly selective H_2 production. Stemming from the same reason, the main reduction product of CB in pure CO_2 atmosphere is H_2 ($384.9 \mu\text{mol g}_{\text{cat}}^{-1} \text{h}^{-1}$) along with a slight amount of CO ($35.1 \mu\text{mol g}_{\text{cat}}^{-1} \text{h}^{-1}$), much similar to the case of CT (Fig. S21).

To further illustrate the impact of OP variation on H_2O oxidation half reaction, LSV measurements of BiVO_4 and T-COF in O_2 evolution reaction were conducted. As depicted in Fig. 6c, BiVO_4 evokes a substantially lower onset potential and a significantly higher anodic current density compared with T-COF. This outcome verifies that BiVO_4 demonstrates more efficient H_2O oxidation kinetics [40]. To gain insight into the mechanism, Gibbs free energy calculation was employed to simulate the H_2O oxidation process in Fig. 6f. For both T-COF and BiVO_4 , the rate-determining step is the conversion of $^*\text{O}$ to $^*\text{OOH}$. Noticeably, the corresponding energy barrier for T-COF is 1.95 eV, larger than that for BiVO_4 (1.80 eV). Hence, the introduction of BiVO_4 endows the CBT with a decreased theoretical overpotential of 0.15 eV, in line with its superior activity in O_2 generation [41]. Additional evidence of this point is that the O_2 evolution rate of CB ($188.9 \mu\text{mol g}_{\text{cat}}^{-1} \text{h}^{-1}$) is 8.2-fold that of hollow CdS (Fig. S21). Besides, the contact angles of water droplets on BiVO_4 and T-COF are 21.24° and 46.97° , respectively (inset of Fig. 6c). The higher hydrophilicity of BiVO_4 also contributes to its superior reactivity in H_2O oxidation [42]. Therefore, it can be concluded that the BiVO_4 insertion not only hoists the transfer and separation efficiency of photoinduced carriers, but also exerts the advantages of each component in maneuvering the surface redox reactions, thereby dramatically enhancing the overall photoactivity in syngas and O_2 production.

Based on the aforementioned results, the photocatalytic reaction mechanism of CBT is proposed in Fig. 6g. In the dual S-scheme heterojunction, the IEFs and upward BB in the outer surface of CdS core and inner surface of T-COF shell drive the flow of photoelectrons away from the interface between them. As a result, H_2 evolves at the inner surface

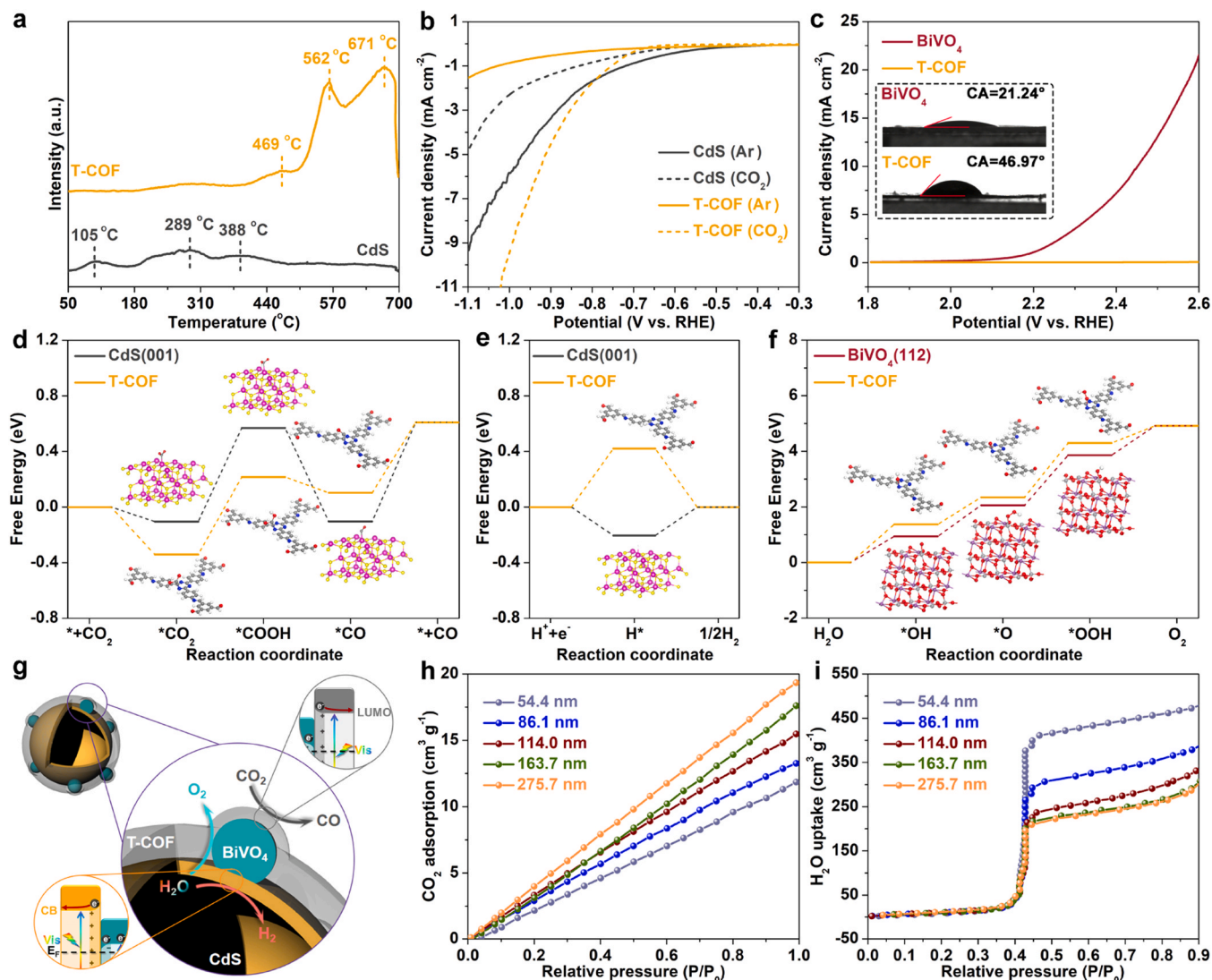


Fig. 6. Surface reaction dynamics analysis of CBT and reference samples: (a) CO₂-TPD profiles; (b,c) LSV curves for (b) CO₂ reduction and (c) H₂O oxidation, (inset of c) water contact angles; (d-f) calculated Gibbs free energy profiles for (d) CO₂ reduction, (e) H₂ evolution and (f) H₂O oxidation; (g) proposed photocatalytic mechanism of CBT; (h) CO₂ and (i) H₂O adsorption isotherms of CBT with different T-COF thicknesses.

of hollow CdS, while CO₂ reduction proceeds on the outer T-COF surface to produce CO. On the other side, downward BB and IEFs confine the holes on the BiVO₄ surface for O₂ generation. As such, the three half reactions take place in different spaces of CBT, impeding the occurrence of reverse reactions [43]. Notably, in spite of the porous nature of T-COF, previous photocatalytic results have revealed that the thickness of which does matter the running of redox reactions beneath the shell. To uncover the mechanism behind the thickness-dependent photocatalytic activity and product selectivity, we investigated the relationship between T-COF thickness and photon harvesting ability of CBT. Interestingly, with the increasing T-COF thickness, the light absorption intensity of CBT gradually declines at the wavelengths longer than the absorption edge of T-COF, elucidating that thicker T-COF coverage induces more serious light shielding on the encapsulated CdS and BiVO₄ (Fig. S22) [44]. Utterly, we studied the influence of T-COF thickness on the mass transport of CO₂ and H₂O molecules. As revealed by CO₂ and water vapor adsorption isotherms in Fig. 6h and i, increasing the T-COF thickness amplifies the CO₂ uptake of CBT, but mitigates their H₂O adsorption capacity. This finding unleashes that thicker shell not only provides more T-COF sites for the adsorption of CO₂ molecules, but also blocks the mass transfer of H₂O molecules and enlarges the diffusion distance of them [45]. Resultantly, the supply of CO₂ molecules to

T-COF sites ascends, and the accessibility of H₂O molecules to CdS and BiVO₄ sites descends. The ever-reduced availability of photon and H₂O not only suppresses the H₂ evolution on CdS and increases the CO/H₂ ratio of syngas, but also impedes the photocarrier recombination in BiVO₄ and retards the hole consumption, which greatly reduces the number of BiVO₄ electrons participating in the S-scheme recombination. In this regard, weak holes of CdS and T-COF cannot be thoroughly consumed, and the surviving ones would recombine with the strong electrons driving the H₂ and CO evolution (Fig. S23). Ultimately, the combination of positive effect in CO₂ enrichment and negative effect in charge recombination determines the volcano-type relationship between the CO output and T-COF thickness.

It is important to note that the hollow structure of CdS is critical to the excellent photoredox catalytic performance of CBT. For comparison, a ternary counterpart with the same architecture as that of CBT was prepared through replacing hollow CdS by non-hollow CdS nanospheres in approximate average diameter, whose H₂, CO and O₂ production rates are 58.9, 63.9 and 49.2 μmol g_{cat}⁻¹ h⁻¹, respectively, significantly lower than those of CBT (Fig. S24). The key advantages of hollow design of CBT include: (i) induces multiple light reflection and scattering in the chamber, (ii) maximizes the interfacial area between the components for S-scheme charge transfer, and (iii) provides the unique inner surface for

the occurrence of H₂ evolution.

4. Conclusion

To summarize, we have demonstrated the construction of a three-in-one artificial photosynthetic system consisting of CO₂ reduction, H₂O oxidation and H₂ evolution components for overall conversion of CO₂ with H₂O to syngas and O₂ based on the transformation of a single-junction S-scheme CT heterojunction to a novel dual S-scheme CBT heterojunction. In the smart design of CBT, hollow CdS core and porous T-COF shell work as RPs for H₂ and CO evolution, respectively, while BiVO₄ embedded into the heterointerface between them serves as an OP for O₂ generation. As the experiments and theoretical calculations revealed, the heterojunction transformation not only magnifies the IEFs and exacerbates the BB, promoting the transfer and separation of active charges for redox reactions, but also alters the function of the components involved, taking full advantages of them to improve the surface reaction kinetics and lower the energy barriers. Resultantly, the optimized CBT photocatalyst exhibits an impressive syngas yield of 453.6 $\mu\text{mol g}_{\text{cat}}^{-1} \text{h}^{-1}$ along with nearly stoichiometric O₂ evolution of 230.5 $\mu\text{mol g}_{\text{cat}}^{-1} \text{h}^{-1}$, 2.0 and 9.5 times as high as those of CT, respectively. Moreover, encouraged by the CO₂ enrichment function of T-COF shell, around 80% of CO evolution rate and selectivity maintain when pure CO₂ is replaced by diluted CO₂ (15%) atmosphere. Additionally, the supply of CO₂, H₂O and photon to different components can be regulated by varying the T-COF thickness of CBT, leading to the tunable CO/H₂ ratios ranging from 1:4.0–3.6:1. Notably, our CBT design brings up another issue that the produced O₂ mixes with the generated syngas, which must be separated before different downstream applications. It is expected that the three-in-one design strategy can be extended to other artificial photosynthetic systems coupling the tunable syngas production with an oxidation half reaction yielding liquid product based on the rational construction of double S-scheme heterojunctions.

CRedit authorship contribution statement

Zhixin Fan: Conceptualization, Investigation, Data curation, Writing - original draft. **Yilin Cai:** Software, Formal analysis, Validation. **Zhenyu Yang:** Conceptualization, Investigation. **Xi Zhang:** Investigation. **Ruowen Shao:** Data curation. **Shuxian Zhong:** Validation, Visualization, Resources. **Leihong Zhao:** Validation, Resources. **Dong Liu:** Validation, Resources. **Song Bai:** Conceptualization, Formal analysis, Supervision, Writing - review & editing, Funding acquisition, Project administration.

Declaration of Competing Interest

The authors declare that they have no known competing financial interests or personal relationships that could have appeared to influence the work reported in this paper.

Data availability

Data will be made available on request.

Acknowledgements

This work was financially supported by the National Natural Science Foundation of China (No. 21603191 and 22279128), Zhejiang Provincial Natural Science Foundation of China (No. LY20B030003 and LQ16B010001), Key Research and Development Program of Zhejiang Province (No. 2023C03148), Public Welfare Technology Application Research Plan Project of Zhejiang Province (Analysis Test Item, No. 2017C37024), Foundation of Science and Technology Bureau of Jinhua (No. 20204185), Gusu Innovation and Entrepreneurship Leading Talents Program (ZXL2022386), and Science and Technology Program of

Suzhou (SWY2022003). The authors would like to thank ShijianjiaLab (www.shijianjia.com) for the KPFM and the contact angle measurements.

Supplementary material available

Fig. S1 ~ Fig. S24 and Table S1 ~ Table S2. This material is available free of charge via the Internet from Elsevier.

Appendix A. Supporting information

Supplementary data associated with this article can be found in the online version at doi:10.1016/j.apcatb.2024.123979.

References

- [1] S. Yoshino, T. Takayama, Y. Yamaguchi, A. Iwase, A. Kudo, CO₂ reduction using water as an electron donor over heterogeneous photocatalysts aiming at artificial photosynthesis, *Acc. Chem. Res.* 5 (2022) 966–977, <https://doi.org/10.1021/acs.accounts.1c00676>.
- [2] T. Kong, Y. Jiang, Y. Xiong, Photocatalytic CO₂ conversion: what can we learn from conventional CO_x hydrogenation, *Chem. Soc. Rev.* 49 (2020) 6579–6591, <https://doi.org/10.1039/c9cs00920e>.
- [3] W. Kim, B.A. McClure, E. Edri, H. Frei, Coupling carbon dioxide reduction with water oxidation in nanoscale photocatalytic assemblies, *Chem. Soc. Rev.* 45 (2016) 3221–3243, <https://doi.org/10.1039/c6cs00062b>.
- [4] S. Bai, J. Jiang, Q. Zhang, Y. Xiong, Steering charge kinetics in photocatalysis: intersection of materials syntheses, characterization techniques and theoretical simulations, *Chem. Soc. Rev.* 44 (2015) 2893–2939, <https://doi.org/10.1039/c5cs00064e>.
- [5] W. Tu, Y. Zhou, Z. Zou, Photocatalytic conversion of CO₂ into renewable hydrocarbon fuels: state-of-the-art accomplishment, challenges, and prospects, *Adv. Mater.* 26 (2014) 4607–4626, <https://doi.org/10.1002/adma.201400087>.
- [6] H. Wang, H. Wang, Z. Wang, L. Tang, G. Zeng, P. Xu, M. Chen, T. Xiong, C. Zhou, X. Li, D. Huang, Y. Zhu, Z. Wang, J. Tang, Covalent organic framework photocatalysts: structures and applications, *Chem. Soc. Rev.* 49 (2020) 4135–4165, <https://doi.org/10.1039/d0cs00278j>.
- [7] Y. Gong, X. Guan, H. Jiang, Covalent organic frameworks for photocatalysis: synthesis, structural features, fundamentals and performance, *Coord. Chem. Rev.* 475 (2022) 214889, <https://doi.org/10.1016/j.ccr.2022.214889>.
- [8] M. Zhang, M. Lu, Z. Lang, J. Liu, M. Liu, J. Chang, L. Li, L. Shang, M. Wang, S. Li, Y. Lan, Semiconductor/covalent-organic-framework Z-scheme heterojunctions for artificial photosynthesis, *Angew. Chem. Int. Ed.* 59 (2020) 6500–6506, <https://doi.org/10.1002/anie.202000929>.
- [9] K. Chen, A. Cai, T. Li, Covalent organic framework-semiconductor-based heterostructures for photocatalytic applications, *ChemSusChem* 16 (2023) e202300021, <https://doi.org/10.1002/cssc.202300021>.
- [10] J. Chen, D. Yuan, Y. Wang, Covalent organic frameworks based heterostructure in solar-to-fuel conversion, *Adv. Funct. Mater.* 33 (2023) 2304071, <https://doi.org/10.1002/adfm.202304071>.
- [11] J. Low, J. Yu, M. Jaroniec, S. Wageh, A.A. Al-Ghamdi, Heterojunction photocatalysts, *Adv. Mater.* 29 (2017) 1601694, <https://doi.org/10.1002/adma.201601694>.
- [12] L. Zhang, J. Zhang, H. Yu, J. Yu, Emerging S-scheme photocatalyst, *Adv. Mater.* 34 (2021) 21076, <https://doi.org/10.1002/adma.202107668>.
- [13] Q. Xu, L. Zhang, B. Cheng, J. Fan, J. Yu, S-scheme heterojunction photocatalyst, *Chem* 6 (2020) 1543–1559, <https://doi.org/10.1016/j.chempr.2020.06.010>.
- [14] F. Xu, K. Meng, B. Cheng, S. Wang, J. Xu, J. Yu, Unique S-scheme heterojunctions in self-assembled TiO₂/CsPbBr₃ hybrids for CO₂ photoreduction, *Nat. Commun.* 11 (2020) 4613, <https://doi.org/10.1038/s41467-020-18350-7>.
- [15] L. Wang, B. Zhu, J. Zhang, J.B. Ghasemi, M. Mousavi, J. Yu, S-scheme heterojunction photocatalysts for CO₂ reduction, *Matter* 5 (2022) 4187–4211, <https://doi.org/10.1016/j.matt.2022.09.009>.
- [16] Y. Wang, Z. Hu, W. Wang, H. He, L. Deng, Y. Zhang, J. Huang, N. Zhao, G. Yu, Y. Liu, Design of well-defined shell-core covalent organic frameworks/metal sulfide as an efficient Z-scheme heterojunction for photocatalytic water splitting, *Chem. Sci.* 12 (2021) 16065–16073, <https://doi.org/10.1039/d1sc05893b>.
- [17] H. Ge, F. Xu, B. Cheng, J. Yu, W. Ho, S-scheme heterojunction TiO₂/CdS nanocomposite nanofiber as H₂-production photocatalyst, *ChemCatChem* 11 (2019) 6301–6309, <https://doi.org/10.1002/cctc.201901486>.
- [18] B. He, P. Xiao, S. Wan, J. Zhang, T. Chen, L. Zhang, J. Yu, Rapid charge transfer endowed by interfacial Ni-O bonding in S-scheme heterojunction for efficient photocatalytic H₂ and imine production, *Angew. Chem. Int. Ed.* 62 (2023) e202313172, <https://doi.org/10.1002/anie.202313172>.
- [19] H.T. Luk, C. Mondelli, D.C. Ferré, J.A. Stewart, J. Pérez-Ramírez, Status and prospects in higher alcohols synthesis from syngas, *Chem. Soc. Rev.* 46 (2017) 1358–1426, <https://doi.org/10.1039/c6cs00324a>.
- [20] P. Zhai, Y. Li, M. Wang, Liu, J. Cao, J. Zhang, Y. Xu, X. Liu, Y. Li, Q. Zhu, D. Xiao, X. Wen, D. Ma, Development of direct conversion of syngas to unsaturated hydrocarbons based on fischer-tropsch route, *Chem* 7 (2021) 3027–3051, <https://doi.org/10.1016/j.chempr.2021.08.019>.

- [21] G. Qian, W. Lyu, X. Zhao, J. Zhou, R. Fang, F. Wang, Y. Li, Efficient photoreduction of diluted CO₂ to tunable syngas by Ni-Co dual sites through d-band center manipulation, *Angew. Chem. Int. Ed.* 61 (2022) e202210576, <https://doi.org/10.1002/anie.202210576>.
- [22] L. Li, X. Dai, D. Chen, Y. Zeng, Y. Hu, X. Lou, Steering catalytic activity and selectivity of CO₂ photoreduction to syngas with hydroxy-rich Cu₂S@ROH-NiCo₂O₃ double-shelled nanoboxes, *Angew. Chem. Int. Ed.* 61 (2022) e202205839, <https://doi.org/10.1002/anie.202205839>.
- [23] W. Mo, Z. Fan, S. Zhong, W. Chen, L. Hu, H. Zhou, W. Zhao, H. Lin, J. Ge, J. Chen, S. Bai, Embedding plasmonic metal into heterointerface of mofs-encapsulated semiconductor hollow architecture for boosting CO₂ photoreduction, *Small* 19 (2023) 2207705, <https://doi.org/10.1002/smll.202207705>.
- [24] T. Sick, J.M. Rotter, S. Reuter, S. Kandambeth, N. Bach, M. Döblinger, J. Merz, T. Clark, T. Marder, T. Bein, D. Medina, Switching on and off interlayer correlations and porosity in 2D covalent organic frameworks, *J. Am. Chem. Soc.* 141 (2019) 12570–12581, <https://doi.org/10.1021/jacs.9b02800>.
- [25] C. Kang, Z. Zhang, V. Wee, A. Usadi, D. Calabro, L. Baugh, S. Wang, Y. Wang, D. Zhao, Interlayer shifting in two-dimensional covalent organic frameworks, *J. Am. Chem. Soc.* 142 (2020) 12995–13002, <https://doi.org/10.1021/jacs.0c03691>.
- [26] P. Wang, Y. Cai, W. Mo, Z. Fan, Z. Li, L. Wu, S. Zhong, S. Bai, Modulating the schottky barrier heights of plasmonic metal/semiconductor heterojunctions by graphene substrates for boosting photocatalytic water oxidation, *Appl. Surf. Sci.* 642 (2023) 158561, <https://doi.org/10.1016/j.apsusc.2023.158561>.
- [27] J. Low, B. Dai, T. Tong, C. Jiang, J. Yu, In situ irradiated X-ray photoelectron spectroscopy investigation on a direct Z-scheme TiO₂/CdS composite film photocatalyst, *Adv. Mater.* 31 (2018) 1802981, <https://doi.org/10.1002/adma.201802981>.
- [28] B. Li, F. Wei, B. Su, Z. Guo, Z. Ding, M. Yang, S. Wang, Mesoporous cobalt tungstate nanoparticles for efficient and stable visible-light-driven photocatalytic CO₂ reduction, *Mater. Today Energy* 24 (2022) 100943, <https://doi.org/10.1016/j.mtener.2022.100943>.
- [29] J. Wang, T. Xia, L. Wang, X. Zheng, Z. Qi, C. Gao, J. Zhu, Z. Li, H. Xu, Y. Xiong, Enabling visible-light-driven selective CO₂ reduction by doping quantum dots: trapping electrons and suppressing H₂ evolution, *Angew. Chem. Int. Ed.* 57 (2018) 16447–16451, <https://doi.org/10.1002/anie.201810550>.
- [30] Y. Wang, Z. Hu, W. Wang, Y. Li, H. He, L. Deng, Y. Zhang, J. Huang, N. Zhao, G. Yu, Y. Liu, Rational design of defect metal oxide/covalent organic frameworks Z-scheme heterojunction for photoreduction CO₂ to CO, *Appl. Catal. B: Environ.* 327 (2023) 122419, <https://doi.org/10.1016/j.apcatb.2023.122419>.
- [31] G. Yang, S. Wang, Y. Wu, H. Zhou, W. Zhao, S. Zhong, L. Liu, S. Bai, Spatially separated redox cocatalysts on ferroelectric nanoplates for improved piezophotocatalytic CO₂ reduction and H₂O oxidation, *ACS Appl. Mater. Interfaces* 15 (2023) 14228–14239, <https://doi.org/10.1021/acsami.2c20685>.
- [32] X. Zhang, Y. Song, X. Niu, X. Lin, S. Zhong, H. Lin, B. Teng, S. Bai, Emerging hollow artificial photosynthetic system with S-scheme heterojunction sandwiched between layered redox cocatalysts for overall CO₂ reduction and H₂O oxidation, *Appl. Catal. B: Environ.* 342 (2024) 123445, <https://doi.org/10.1016/j.apcatb.2023.123445>.
- [33] X. Ruan, C. Huang, H. Cheng, Z. Zhang, Y. Cui, Z. Li, T. Xie, K. Ba, H. Zhang, L. Zhang, X. Zhao, J. Leng, S. Jin, W. Zhang, W. Zheng, S. Ravi, Z. Jiang, X. Cui, J. Yu, A twin S-scheme artificial photosynthetic system with self-assembled heterojunctions yields superior photocatalytic hydrogen evolution rate, *Adv. Mater.* 35 (2022) 2209141, <https://doi.org/10.1002/adma.202209141>.
- [34] P. Xia, X. Pan, S. Jiang, J. Yu, B. He, P.M. Ismail, W. Bai, J. Yang, L. Yang, H. Zhang, M. Cheng, H. Li, Q. Zhang, C. Xiao, Y. Xie, Designing a redox heterojunction for photocatalytic “overall nitrogen fixation” under mild conditions, *Adv. Mater.* 34 (2022) 2200563, <https://doi.org/10.1002/adma.202200563>.
- [35] A. Wang, M. Du, J. Ni, D. Liu, Y. Pan, X. Liang, D. Liu, J. Ma, J. Wang, W. Wang, Enhanced and synergistic catalytic activation by photoexcitation driven S-scheme heterojunction hydrogel interface electric field, *Nat. Commun.* 14 (2023) 6733, <https://doi.org/10.1038/s41467-023-42542-6>.
- [36] P. Li, G. Luo, S. Zhu, L. Guo, P. Qu, T. He, Unraveling the selectivity puzzle of H₂ evolution over CO₂ photoreduction using ZnS nanocatalysts with phase junction, *Appl. Catal. B: Environ.* 274 (2020) 119115, <https://doi.org/10.1016/j.apcatb.2020.119115>.
- [37] S. Wang, Z. Li, G. Yang, Y. Xu, Y. Zheng, S. Zhong, Y. Zhao, S. Bai, Embedding nano-piezoelectrics into heterointerfaces of S-scheme heterojunctions for boosting photocatalysis and piezophotocatalysis, *Small* 19 (2023) 2302717, <https://doi.org/10.1002/smll.202302717>.
- [38] X. Zhang, P. Wang, X. Lv, X. Niu, X. Lin, S. Zhong, D. Wang, H. Lin, J. Chen, S. Bai, Stacking engineering of semiconductor heterojunctions on hollow carbon spheres for boosting photocatalytic CO₂ reduction, *ACS Catal.* 12 (2022) 2569–2580, <https://doi.org/10.1021/acscatal.1c05401>.
- [39] W. Zhao, W. Mo, Y. Zhang, L. Hu, Y. Zheng, Z. Chen, X. Niu, Y. Zhao, L. Liu, S. Zhong, S. Bai, Bifunctional noble-metal-free cocatalyst coating enabling better coupling of photocatalytic CO₂ reduction and H₂O oxidation on direct Z-scheme heterojunction, *Nano Res.* (2024), <https://doi.org/10.1007/s12274-024-6514-8>.
- [40] S. Anantharaj, S. Kundu, Do the evaluation parameters reflect intrinsic activity of electrocatalysts in electrochemical water splitting, *ACS Energy Lett.* 4 (2019) 1260–1264, <https://doi.org/10.1021/acsenenergylett.9b00686>.
- [41] T. Jing, D. Liang, M. Deng, S. Cai, X. Qi, Density functional theory studies of heteroatom-doped graphene-like gan monolayers as electrocatalysts for oxygen evolution and reduction, *ACS Appl. Nano Mater.* 4 (2021) 7125–7133, <https://doi.org/10.1021/acsnm.1c01119>.
- [42] S.D. Ghadge, O.I. Velikokhatnyi, M.K. Datta, P.M. Shanthi, S. Tan, K. Damodaran, P.N. Kumta, Experimental and theoretical validation of high efficiency and robust electrocatalytic response of one-dimensional (1D) (Mn,Ir)O₂:10F nanorods for the oxygen evolution reaction in PEM-based water electrolysis, *ACS Catal.* 9 (2019) 2134–2157, <https://doi.org/10.1021/acscatal.8b02901>.
- [43] Y. Yang, H. Zhang, Y. Wang, L. Shao, L. Fang, H. Dong, M. Lu, L. Dong, Y. Lan, F. Zhang, Integrating enrichment, reduction, and oxidation sites in one system for artificial photosynthetic diluted CO₂ reduction, *Adv. Mater.* 35 (2023) 2304170, <https://doi.org/10.1002/adma.202304170>.
- [44] S. Wang, Y. Zhang, Y. Zheng, Y. Xu, G. Yang, S. Zhong, Y. Zhao, S. Bai, Plasmonic metal mediated charge transfer in stacked core-shell semiconductor heterojunction for significantly enhanced CO₂ photoreduction, *Small* 19 (2022) 2204774, <https://doi.org/10.1002/smll.202204774>.
- [45] H. Lyu, H. Li, N. Hanikel, K. Wang, O.M. Yaghi, Covalent organic frameworks for carbon dioxide capture from air, *J. Am. Chem. Soc.* 144 (2022) 12989–12995, <https://doi.org/10.1021/jacs.2c05382>.